

Article

High-Cycle Fatigue Behaviour of the Aluminium Alloy 5083-H111

Branko Nečemer, Franc Zupanič , Tomaž Vuherer and Srečko Glodež * 

Faculty of Mechanical Engineering, University of Maribor, Smetanova 17, 2000 Maribor, Slovenia

* Correspondence: srecko.glodez@um.si

Abstract: This study presents a comprehensive experimental investigation of the high-cycle fatigue (HCF) behaviour of the ductile aluminium alloy AA 5083-H111. The analysed specimens were fabricated in the rolling direction (RD) and transverse direction (TD). The HCF tests were performed in a load control (load ratio $R = 0.1$) at different loading levels under the loading frequency of 66 Hz up to the final failure of the specimen. The experimental results have shown that the S–N curves of the analysed Al-alloy consist of two linear curves with different slopes. Furthermore, RD-specimens demonstrated longer fatigue life if compared to TD-specimens. This difference was about 25% at the amplitude stress 65 MPa, where the average fatigue lives 276,551 cycles for RD-specimens, and 206,727 cycles for TD-specimens were obtained. Similar behaviour was also found for the lower amplitude stresses and fatigue lives between 10^6 and 10^8 cycles. The difference can be caused by large $Al_6(Mn,Fe)$ particles which are elongated in the rolling direction and cause higher stress concentrations in the case of TD-specimens. The micrography of the fractured surfaces has shown that the fracture characteristics were typical for the ductile materials and were similar for both specimen orientations.

Keywords: aluminium alloys; rolling direction; high-cycle fatigue; fracture analysis



Citation: Nečemer, B.; Zupanič, F.; Vuherer, T.; Glodež, S. High-Cycle Fatigue Behaviour of the Aluminium Alloy 5083-H111. *Materials* **2023**, *16*, 2674. <https://doi.org/10.3390/ma16072674>

Academic Editor: Qianhua Kan

Received: 30 January 2023

Revised: 16 March 2023

Accepted: 22 March 2023

Published: 28 March 2023



Copyright: © 2023 by the authors. Licensee MDPI, Basel, Switzerland. This article is an open access article distributed under the terms and conditions of the Creative Commons Attribution (CC BY) license (<https://creativecommons.org/licenses/by/4.0/>).

1. Introduction

Aluminium alloy series 5xxx is a group of alloys based on aluminium–magnesium (Al–Mg) compositions [1]. These alloys are known for their high strength-to-weight ratio, excellent corrosion resistance, and good formability [2–4]. Based on these characteristics and their mechanical properties, these alloys are used widely in the automotive and aerospace industries, transportation, and other applications where lightweight and corrosion-resistant materials are required [5–9].

In the past, numerous studies have been conducted to understand the fatigue behaviour of AA 5xxx alloys [10–14]. Fatigue is an essential factor in determining the behaviour of mechanical parts under variable loads and is the primary cause of 80–90% of engineering failures. In applications that use aluminium alloys frequently, it is necessary to understand the fatigue performance of the components and the effects of operating parameters on the fatigue behaviour of the analysed constructional components. A fatigue assessment can be carried out using the stress–life (S–N) or the strain–life approach, depending on whether stresses in the critical cross-sections of the analysed component are in the elastic or plastic areas [15,16]. In the case that only elastic stresses occur, the S–N approach is usually used to obtain the fatigue life up to the final failure of the component. Establishing comprehensive databases, including S–N information, is essential for evaluating the fatigue characteristics of components under different operating conditions accurately. The fatigue life of Al-alloys is influenced not only by material characteristics but also by the characteristics of the specimens, such as microcavities formed during production, surface defects, hot or cold deformation, and changes in grain structure [17–19]. The tensile strength and fatigue life of Al-alloys are affected slightly by the rolling direction

at room temperature, but the effects become more significant at higher temperatures due to the expansion of the grain structure [20,21]. Hockauf et al. [22] investigated the effect of different precipitate morphologies on low-cycle fatigue (LCF) and fatigue crack growth in an ultrafine-grained (UFG) age-hardening aluminium alloy. Their experimental results showed that the newly formed, coherent precipitates in the thermally recovered condition contribute to more planar slip behaviour, slip localisation and early failure during LCF loading. In [23], the researchers investigated the high-cycle fatigue behaviour of an Al-Si-Cu-Mn aluminium alloy at room temperature and 350 °C and evaluated the effect of different second phases on its fatigue behaviour. The alloy demonstrated excellent fatigue resistance at both temperatures, with a high-cycle fatigue strength of 125.0 MPa at room temperature and 47.5 MPa at 350 °C. The study found that fatigue cracks in the alloy at room temperature originated from casting defects, while at 350 °C, they nucleated from the primary Al-Mn-Si phase on the specimen's surface. The study also demonstrated that the modulus difference between the Al-Mn-Si phase and the alpha aluminium phase was higher at 350 °C than at room temperature, leading to more crack initiation and propagation along the phase interface at 350 °C. Khisheh et al. [24] investigated the influences of surface roughness and heat treatment on the high-cycle bending fatigue properties of A380 aluminium alloy under stress-controlled cyclic loading. The results showed that the heat treatment increased the high-cycle bending fatigue lifetime by 26% (for the highest stress level) and 85% (for the lowest stress level), respectively. The study also found that samples with low roughness had a longer fatigue life than those with high roughness. In the research presented by Gao et al. [25], the authors investigated the effect of surface mechanical attrition treatment (SMAT) on the fatigue performance of a 7075-T6 aluminium alloy in both high-cycle fatigue (HCF) and very-high-cycle fatigue (VHCF) regimes. The results showed that SMAT could improve fatigue strength in the HCF regime but decrease it in the VHCF regime. Meng et al. [26] investigated the vibration fatigue improvement of 2024-T351 aluminium alloy by ultrasonic-assisted laser shock peening (ULP). The results showed that the ULP increases the dislocation density significantly and refines the grains, leading to increased compressive residual stress and microhardness and inhibited crack initiation and propagation, resulting in a significant increase in vibration fatigue life. Xing et al. [27] studied the transition fatigue failure of weld toe cracking and weld root cracking in aluminium fillet welds. Their experimental results showed that the weld root cracking has a lower fatigue life and wider scatter band than the weld toe cracking. The researchers also proposed the weld sizing criterion for avoiding weld root cracking in fillet-welded aluminium connections. Sakin et al. [28] investigated the bending fatigue lives of AA 1100 and AA 1050 aluminium sheets experimentally under both high-cycle fatigue (HCF) and low-cycle fatigue (LCF) conditions. The specimens were tested along four different directions, including the rolling direction (RD) and transverse direction (TD). The results showed that the longest fatigue lives in the LCF region were observed in the AA1050 (RD) specimens, while the AA 1100 (RD) specimens had the longest fatigue lives in the HCF region. In the research works presented in [29–32], the researchers investigated the fatigue behaviour of cellular structures made of different aluminium sheets. The specimens were fabricated in a rolling direction using water jet cutting technology.

Material testing provides valuable information on the material's mechanical properties, such as its stress–strain response, deformation, fatigue life, and fracture behaviour. This information is crucial for optimising the design and manufacture of engineering structures and components made from this material and assessing their performance and durability in various applications. The proposed study is the continuation of the author's previous work [33], where the LCF behaviour of the aluminium alloy 5083-H111 was investigated. The obtained experimental results (cyclic S–N curve, LCF-fatigue parameters) were then used in work [34], where Nečemer et al. analysed the LCF behaviour of auxetic cellular structures. As presented by Lehmus et al. [35], cellular structures represent a unique opportunity for adoption in lightweight design due to their favourable characteristics regarding sound isolation, damping, energy absorption, etc. Using the

advanced additive manufacturing (AM) technologies, abrasive water jet (AWJ) cutting technology, etc., different types of cellular structures (see two examples in Figure 1) can be manufactured for specific mechanical properties and other characteristics useful for different engineering applications. When analysing the fatigue behaviour of cellular structures made of aluminium alloy AA 5083-H111, the effect of rolling direction on the fatigue life may be significant, especially in the high-cycle fatigue (HCF) area. For that reason, the proposed research considers the influence of the rolling direction on the fatigue life and fracture behaviour of aluminium alloy AA 5083-H111 in the HCF regime. Additionally, the obtained results could help engineers make the appropriate decisions about the use and performance of this alloy in various engineering applications.

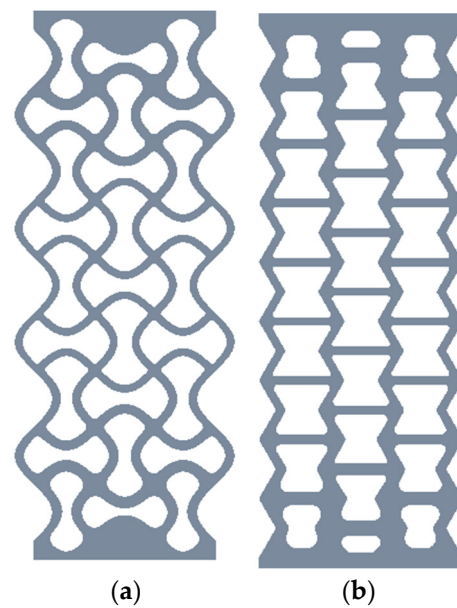


Figure 1. Two examples of cellular structures: (a) chiral structure; (b) re-entrant structure.

2. Materials and Methods

2.1. Material and Specimen Geometry

In the experimental investigation, the specimens were made from the aluminium alloy AA 5083-H111, which is a commonly used aluminium alloy known for its excellent corrosion resistance and high strength-to-weight ratio. The chemical composition of this alloy is presented in Table 1.

Table 1. The chemical composition of AA 5083-H111.

Al [wt %]	Mg [wt %]	Mn [wt %]	Si [wt %]	Fe [wt %]	Zn [wt %]	Cr [wt %]	Ti [wt %]	Cu [wt %]
92.55	4.9	1	0.4	0.4	0.25	0.25	0.15	0.1

The flat tensile specimen shown in Figure 2a, taken from one batch of material, was used in the uniaxial quasi-static tensile tests and high-cycle fatigue (HCF) tests. All the specimens were fabricated using the abrasive water jet (AWJ) cutting technology from a 4 mm thick sheet. The specimens were fabricated in the rolling direction (RD) and transverse direction (TD); see Figure 2b.

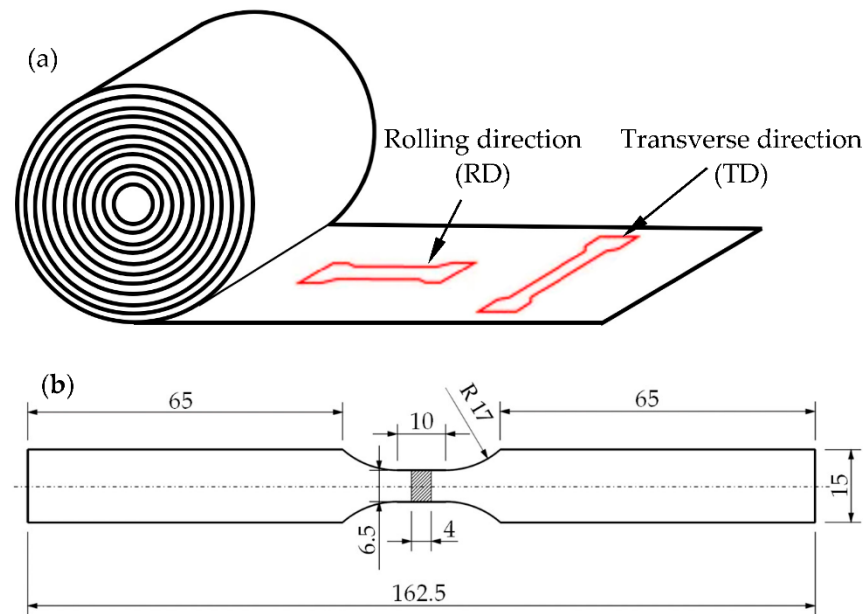


Figure 2. (a) Specimen's orientations. (b) Geometry and dimensions of the specimen.

Figure 3 shows the backscattered electron images of the investigated alloy in its as-received condition for both orientations (in the rolling and transverse directions). The alloy is composed of an Al-rich solid solution, alpha-Al, dark Mg_2Si particles, large bright iron-rich $Al_6(Fe, Mn)$ particles, and smaller plate-like Mn-rich $Al_6(Fe, Mn)$ particles. The particles were identified using EDS. A detailed investigation of particles was carried out in our previous publication [33], and the results were consistent with the findings of Liu et al. [13]. The microstructures in both sections are very similar; however, the dimensions of Fe-rich $Al_6(Fe, Mn)$ particles are longer in the direction of rolling.

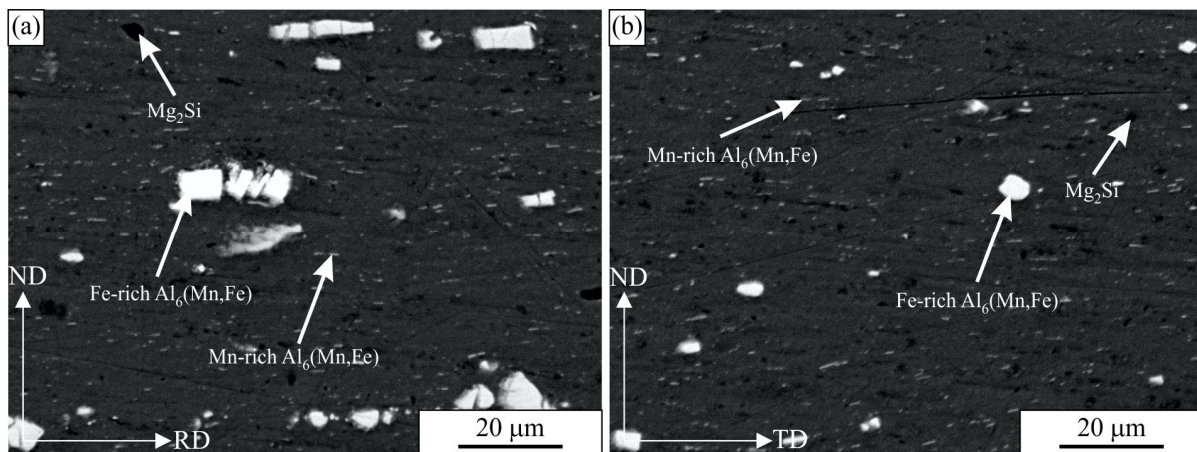


Figure 3. The backscattered electron images of the AA 5083-H111 alloy. (a) In the longitudinal direction. (b) In the transverse direction: RD-rolling direction, ND-normal direction, TD-transverse direction.

2.2. Experimental Methods

In the scope of the experimental investigation, the quasi-static tensile tests were performed, as well as the HCF tests. All the tests were carried out on the electrodynamic pulsating testing machine Vibrophore 100 ZwickRoell.

The quasi-static tensile tests were performed in a force control at an ambient temperature of 22 °C. The force was monitored with a 100 kN tensile–compressive load cell

mounted on the testing machine, while the strain was controlled on the narrowed part of the specimen with an axial mechanical extensometer ZwickRoell DigiClip 40. Four quasi-static tensile tests were performed for each specimen orientation.

The HCF tests were performed in load control at different load levels at the same ambient temperature of 22 °C. The loading frequency was fixed to 66 Hz considering the sinusoidal wave shape with the constant load ratio $R = 0.1$. In the experimental testing, eight different values of maximum force F_{max} were selected for each specimen orientation. The first stress level (maximum force F_{max}) was defined at approximately 50% of the yield stress of the material, and each next stress level was reduced by 3 %. At least two or three specimens were tested for each stress level, up to the final failure of the specimen. The run-out condition (without failure) was set to 10^8 cycles.

The metallographic samples were prepared by grinding with SiC paper and polished using diamond paste. They were examined using the scanning electron microscope (SEM) Quanta 3D (FEI, Eindhoven, the Netherlands). The fractography study was carried out using a light microscope, an Olympus EP 50, and the aforementioned SEM. The micro-chemical analysis of the particles in a scanning electron microscope Sirion 400 NC (FEI, Eindhoven, The Netherlands) equipped with an energy-dispersive spectrometer (Oxford Analytical, Bicester, UK).

3. Results and Discussion

3.1. Quasi-Static Tensile Tests

Figure 4 shows the engineering stress–strain curves for both specimens' layouts. The average mechanical properties of the analysed aluminium alloy AA 5083-H111 are summarised in Table 2. The Young's modulus for the rolling direction (RD) was evaluated at around 70.8 GPa, while, for the transverse direction (TD), it was around 71.2 GPa. Furthermore, the yield stress and ultimate tensile strength were found to be higher for the RD if compared to the TD. Finally, the strain at fracture was found to be almost the same for both specimens' orientations.

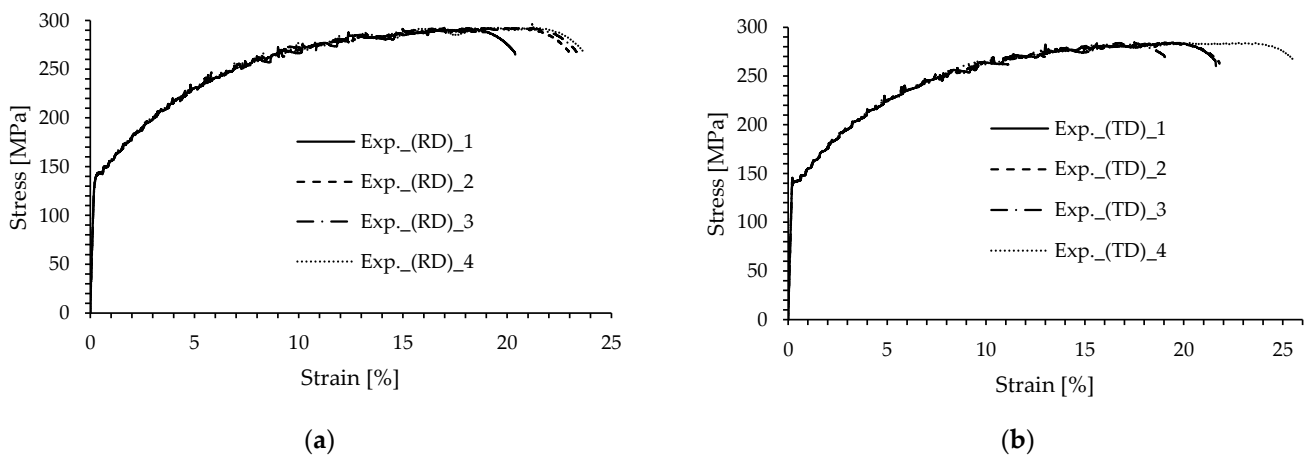


Figure 4. Engineering stress–strain curves of the AA 5083-H111 alloy. (a) Rolling direction (RD). (b) Transverse direction (TD).

Table 2. Average mechanical properties of AA 5083-H111.

Young's Modulus E [GPa]		Yield Stress σ_y [MPa]		UTS σ_{UTS} [MPa]		Elongation A [%]	
(RD)	(TD)	(RD)	(TD)	(RD)	(TD)	(RD)	(TD)
70.8	71.2	143.2	141.9	293.9	284.2	22.2	21.9

(RD)—rolling direction, (TD)—transverse direction.

Based on the experimental results presented in Figure 4 and Table 2, it can be concluded that the mechanical properties (Young's modulus, yield stress, ultimate tensile strength, elongation at fracture) were quite similar for both specimens. However, the specimens manufactured in the longitudinal/rolling direction demonstrated slightly better properties (except for Young's modulus, E) if compared to the specimens manufactured perpendicular to the rolling direction (transverse direction).

Figure 5 shows the fractured surfaces of the tensile specimens for both directions. The elongation at fracture was about 18%, while the contraction was very low. The fracture surface was inclined about 45° in relation to the loading direction. The fracture shows a ductile character with many dimples. The diameters of the larger pores were 20 to 30 μm , and the smaller ones were a few micrometres. Inside the larger voids, coarse intermetallic particles were present. Inside the smaller pores, some particles were found occasionally. Thus, the pores started to form at the interfaces between the matrix and intermetallic particles. In addition, some of the larger particles also fractured during deformation. The pore sizes were several times larger than the particle sizes.

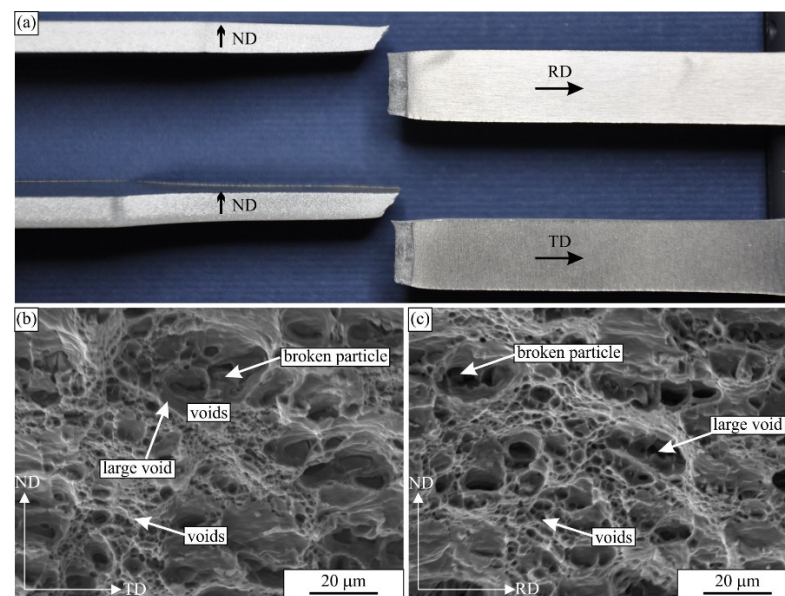


Figure 5. The fractured tensile specimens. (a) The photography of the samples. The secondary electron micrographs of the fractured surfaces of the tensile specimens: (b) in the RD and (c) in the TD.

3.2. High-Cycle Fatigue Tests

The high-cycle fatigue (HCF) tests were performed in a force control under pulsating loading (load ratio $R = 0.1$) at a constant frequency of 66 Hz. Eight loading levels were selected, to obtain the S–N curves for both specimens' layouts. The S–N curves presented in Figures 6 and 7 were defined by plotting the stress amplitude σ_a versus the number of cycles to failure N_f . Some scatter of the experimental results presented in Figures 6 and 7 is evident for both specimens' layouts. However, the scatter is greater for the transverse direction. Furthermore, the S–N curves are "bilinear" and consist of two linear curves with different slopes, which intersect at the knee point N_k [36]. The fatigue behaviour below and upper the knee point N_k can be expressed as follows:

$$\sigma_a = \sigma_{a,k} \cdot \left(\frac{N_k}{N_f} \right)^{\frac{1}{k}} \quad \text{below the knee point} \quad (1)$$

$$\sigma_a = \sigma_{a,k} \cdot \left(\frac{N_k}{N_f} \right)^{\frac{1}{k^*}} \quad \text{above the knee point} \quad (2)$$

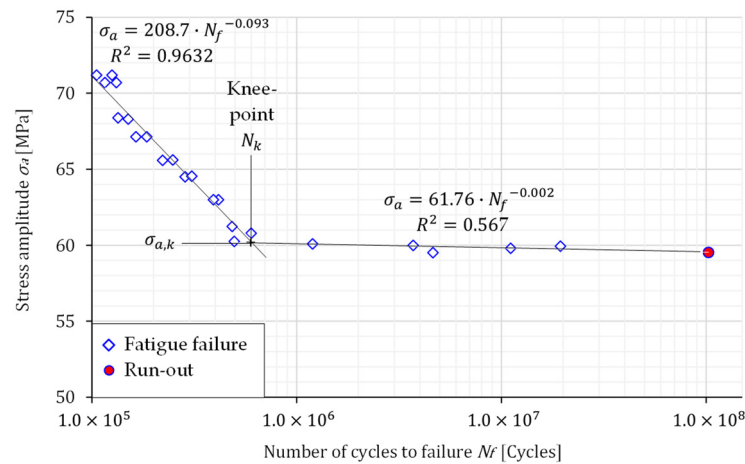


Figure 6. The S–N curve for the rolling direction.

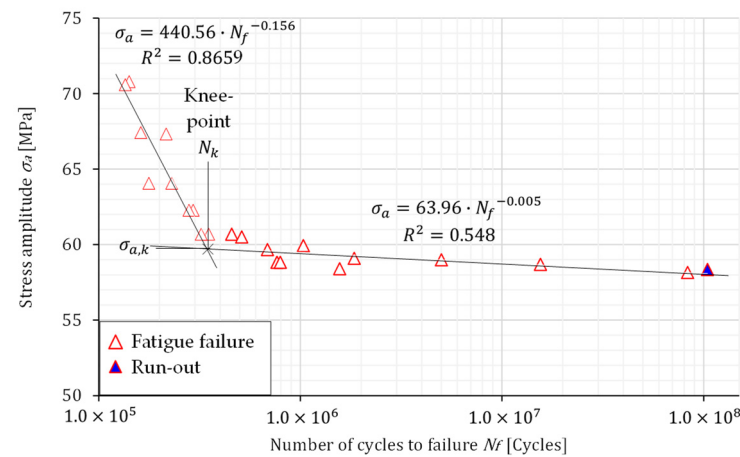


Figure 7. The S–N curve for the transverse direction.

In Equations (1) and (2), the k represents the slope before the knee point, $\sigma_{a,k}$ is the stress amplitude at the knee point, N_k is the number of cycles at the knee point, k^* is the slope after the knee point, and σ_a is the amplitude stress. The material parameters related to the Equations (1) and (2) are summarised in Table 3.

Table 3. Fatigue parameters of AA 5083-H111 related to the bilinear S–N curve.

Number of Cycles at the Knee Point N_k [Cycles]		Stress Amplitude at the Knee Point $\sigma_{a,k}$ [MPa]		Slope before the Knee Point k [1]		Slope after the Knee Point K^* [1]	
(RD)	(TD)	(RD)	(TD)	(RD)	(TD)	(RD)	(TD)
596,500	348,500	60.2	59.7	10.02	6.14	389.04	199.5

(RD)—rolling direction; (TD)—transverse direction.

Figure 8 shows the comparison of S–N curves for both specimen layouts. It is clear that the amplitude stress of the knee point, $\sigma_{a,k}$, is almost the same for both specimen layouts. However, the number of cycles of the knee point is higher for the specimens

oriented in the rolling direction, which is then reflected in the slopes k and k^* . When analysing the fatigue live for both specimen orientations, it is evident from Figures 6–8 that RD-specimens demonstrate longer fatigue live if compared to the TD-specimens. This difference is about 25 % at the amplitude stress 65 MPa, where fatigue lives 276,551 cycles for RD-specimens, and 206,727 cycles for TD-specimens were obtained. Similar behaviour may also be found for the lower amplitude stresses and fatigue lives between 10^6 and 10^8 cycles. The difference can be caused by large $Al_6(Mn,Fe)$ particles which are elongated in the rolling direction and cause higher stress concentrations in the case of TD-specimens.

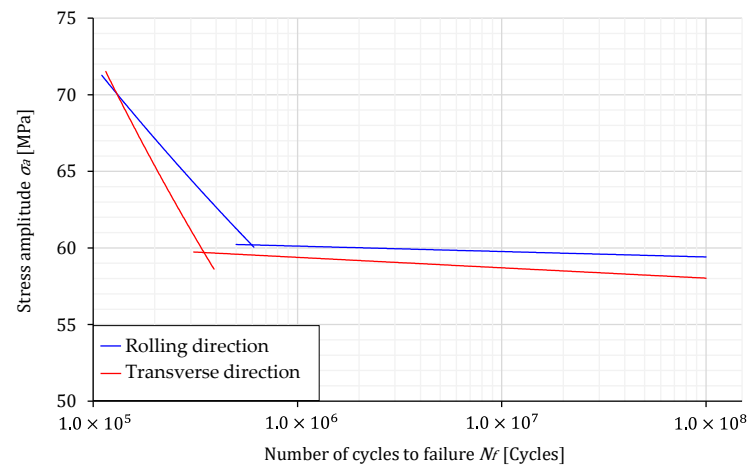


Figure 8. The comparison of S–N curve for both specimen’s directions.

Figure 9 shows the fractured surfaces of the selected fatigue specimens. The cracks are typically initiated at specimen edges and then propagated in the directions indicated by the arrows. As can be seen, they propagated in the direction parallel to the original sheet surface. In our case, the cracks started at a corner at the top and then propagated towards the bottom.



Figure 9. The light micrographs of the fractured surfaces of the selected fatigue samples: (a,c) longitudinal layout and (b,d) transverse layout (ND—normal direction, RD—rolling direction, TD—transverse direction).

The initial parts of the cross-sections were relatively flat and approximately normal to the loading direction. At some distances, the fracture surface became rougher, and this coincided with the distortion of the specimen in the bottom part caused by the plastic deformation. The initially rectangular shape became distorted, and the distortion was higher at higher stress levels for the samples on the left side of the images.

Figures 10 and 11 show the scanning electron micrographs of the fracture surfaces of the selected specimens at three different positions. The fracture characteristics were similar irrespective of the sample orientation (longitudinal or transverse layout) and the number of cycles to fracture. At the beginning of the cracks, the surface was rough on the micrometre scale. The crack followed the glide planes in the grains and formed rather flat facets [37]. Striations were present on the facets. The distances between them were less than one micrometre, typically between 0.4 and 0.7 μm (see Figure 12a).

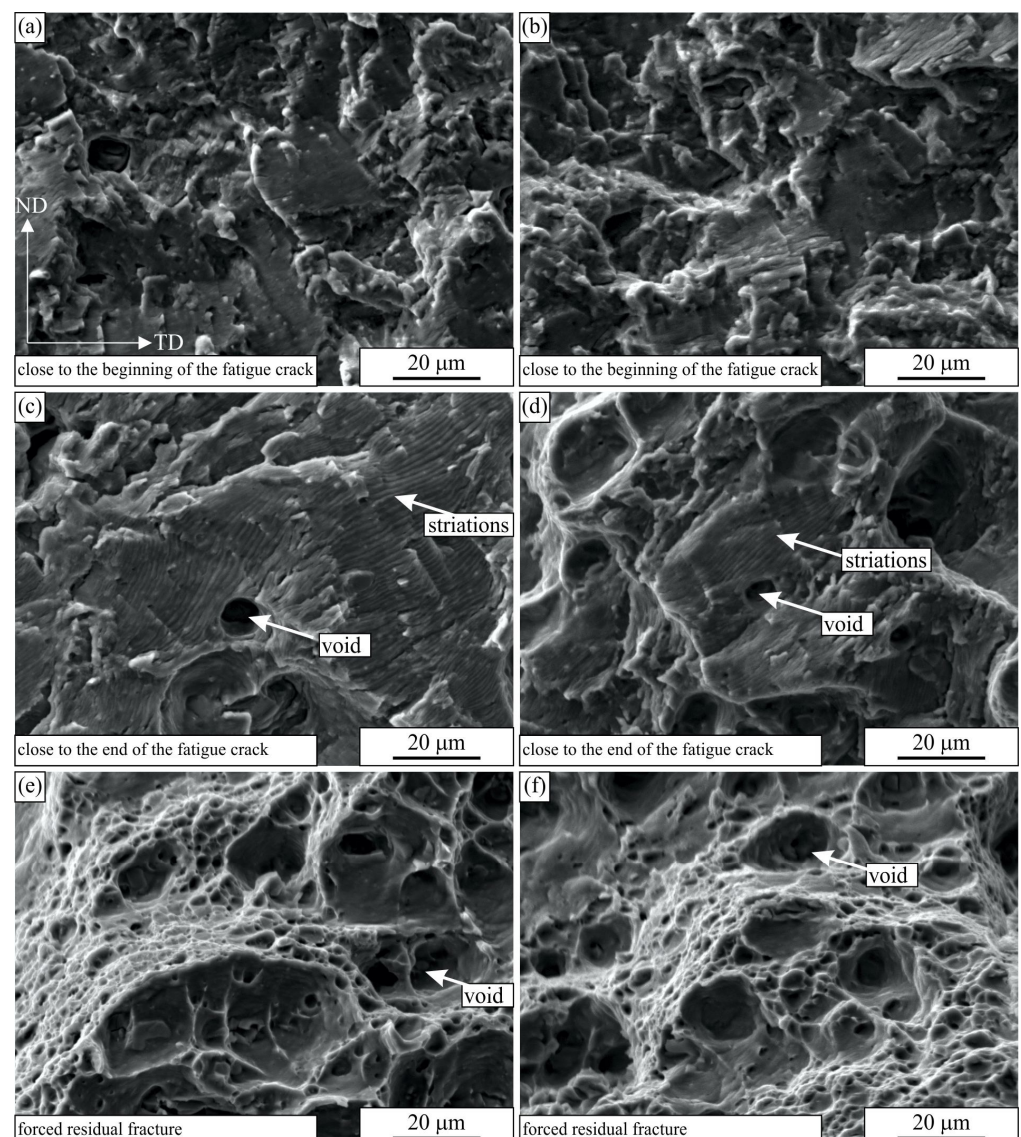


Figure 10. The secondary electron micrographs of the fractured surfaces of the fatigue samples tested in the longitudinal layout: (a,c,e) SV 15 (131,581 cycles to failure), (b,d,f) SV 19 (19,392,180 cycles to failure). The orientation of all images is the same. The RD direction is perpendicular to the images.

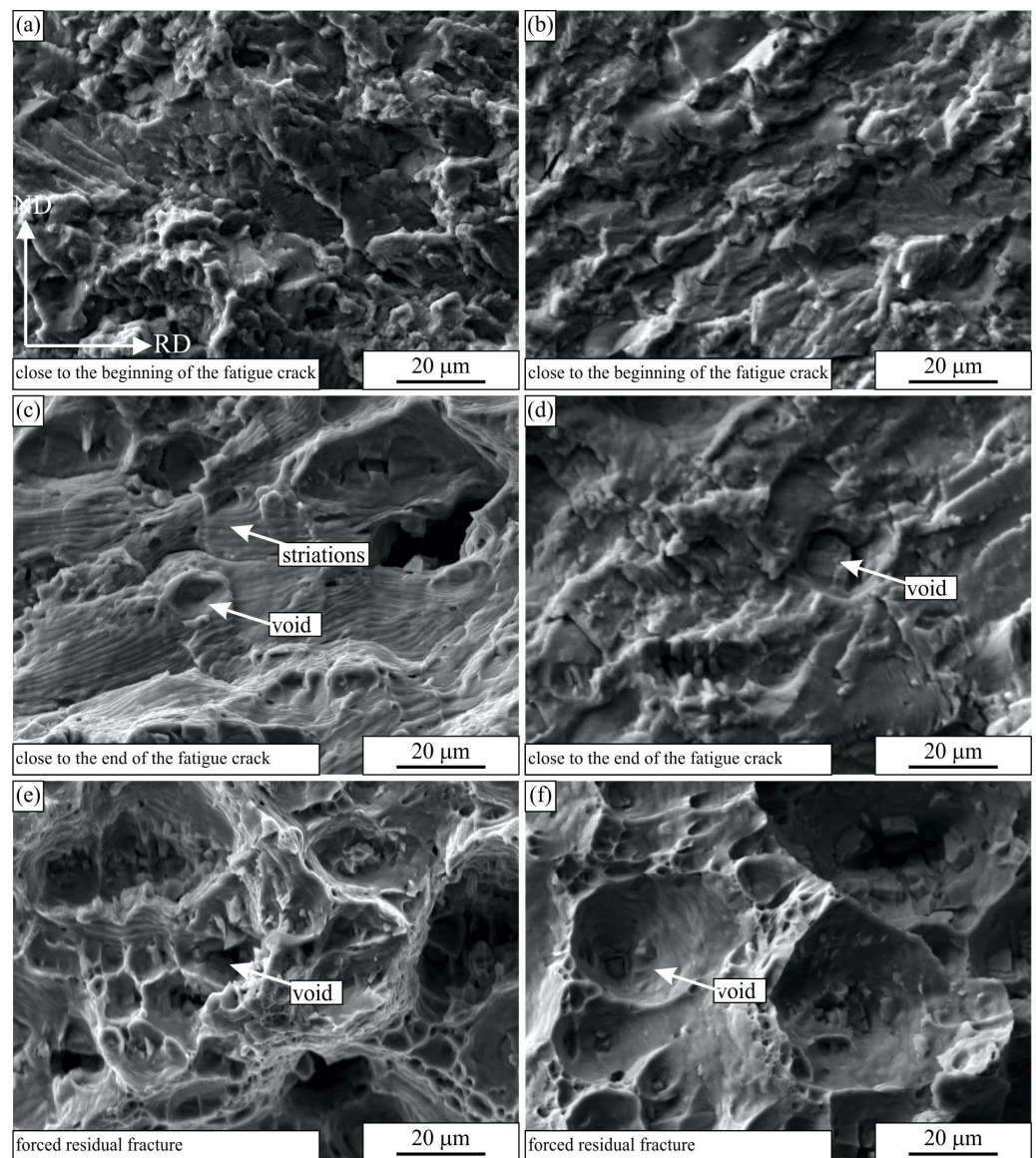


Figure 11. The secondary electron micrographs of the fractured surfaces of the fatigue samples tested in the transverse layout: (a,c,e) PSV 18 (135,165 cycles to failure), (b,d,f) SV 10 (15,500,000 cycles to failure). The orientation of all images is the same. The TD direction is perpendicular to the images.

In the last stages of the crack propagation, the surface was rather rough, and it was not perpendicular to the loading direction. The distances between striations increased and were typically between 2 and 4 μm . In these regions, not only striations were present, but also some voids. The voids formed at larger inclusions in the microstructure. They formed in the regions in front of the fatigue crack as the stresses surpassed the yield stress of the material, and they grew until the main fatigue crack overtook them. The final forced residual fracture was almost the same as the tensile fracture (see Figure 3) and consisted of voids of different sizes.

Figure 12 shows some fractured surfaces at a much higher magnification and resolution. The distances between the striations—the striation wavelengths—were measured on the basis of such micrographs. They are presented in Figure 13. The striations were not visible up to distances below 1 mm from the crack initiation site (Figure 12a), which was typically at the specimen corner. This is Region A of crack propagation, which is highly sensitive to microstructure characteristics [38]. Usually, a crack with a length 1–2 mm is considered a small fatigue crack. One can observe grain boundaries and facets in the crystal grains,

which typically glide planes. The crack propagation rate is often in the order of nm, and the specimen survives in this region for most of its lifetime [39]. Striations become visible in range B of crack propagation [38]. The striations become stable, and in the first part, their wavelength is in the order of 100 nm; we measured 200 nm at a distance of 1.4 mm from the crack initiation site (Figure 12b).

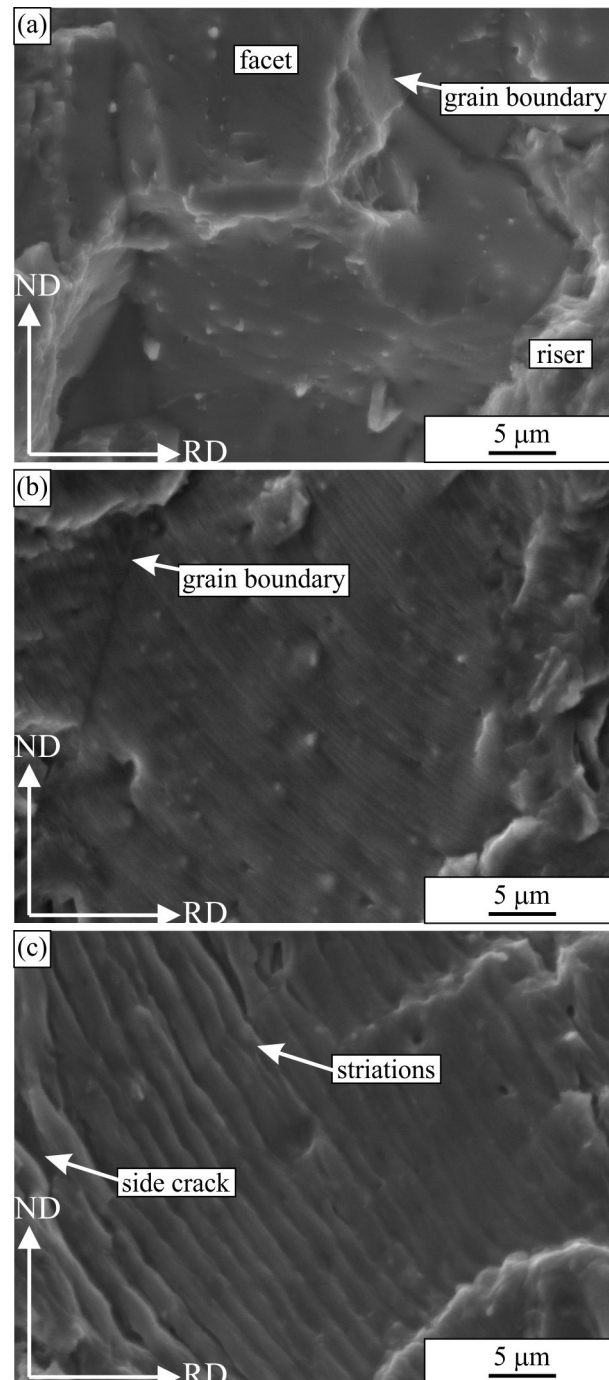


Figure 12. Secondary electron micrographs of the fractured surfaces of the fatigue sample PSV 14 (765,121 cycles to failure): (a) 0.7 mm from the fatigue crack initiation (Stage Regime A), (b) 1.4 mm from the fatigue crack initiation (start of Regime B), (c) 3.5 mm from the fatigue crack initiation (near the end of Regime B).

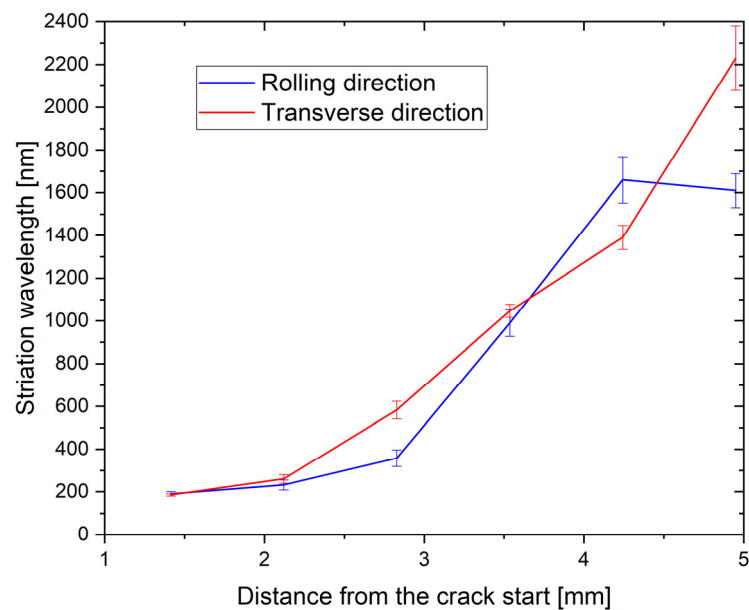


Figure 13. Striation wavelength in dependence from the crack start (RD—sample, TD—sample).

With the growing fatigue crack, the stress intensity factor grows, and the striation wavelength increases in micrometre size. It should be stressed that with the wavelength of 1 μm , the fatigue crack will proceed 1 mm after 1000 cycles and leads to a quick fracture of the specimen. This wavelength was achieved approximately 3.5 mm from the crack initiation (Figure 12c). In Regime B, the crack propagation is less sensitive to microstructure. During the main part of the crack path, the distances between the striations were larger for the transverse specimen, which can also explain the shorter lifetime for this specimen. The last two measurements were close to the crack ends, where the surface resembled those to that shown in Figure 10c,d and Figure 11c,d, where the scatter was rather large. At the transition from Regime B to Regime C, the crack propagation becomes more microstructure sensitive. In the case of this alloy, fatigue cracks can form even in the front of the main cracks around the largest inclusions, as was discussed before.

4. Conclusions

The comprehensive experimental investigation of the high-cycle fatigue (HCF) behaviour of the ductile aluminium alloy AA 5083-H111 was presented in this study. Based on the metallographic investigation of the material, quasi-static tensile tests, high-cycle fatigue tests, and fractography of the fractured surfaces of the quasi-static and fatigue specimens, the following conclusions can be made:

- The analysed AA 5083-H111 alloy is composed of an Al-rich solid solution, alpha-Al, dark Mg_2Si particles, large bright iron-rich $\text{Al}_6(\text{Fe}, \text{Mn})$ particles, and smaller, plate-like Mn-rich $\text{Al}_6(\text{Fe}, \text{Mn})$ particles. The microstructures in both the longitudinal/rolling (RD) and transversal (TD) directions were found to be very similar. However, the dimensions of the Fe-rich $\text{Al}_6(\text{Fe}, \text{Mn})$ particles were longer in the longitudinal/rolling direction.
- The mechanical properties (yield stress, ultimate tensile strength, elongation at fracture) were quite similar for both specimens. However, the specimens manufactured in the longitudinal/rolling direction demonstrated slightly better properties (except for Young's modulus, E) if compared to the specimens manufactured perpendicular to the rolling direction (transverse direction).
- The experimental results have shown that the S–N curves of the analysed Al-alloy consist of two linear curves with different slopes, which intersect at the knee point N_k . The corresponding amplitude stress at the knee point, $\sigma_{a,k}$, was found to be almost the same for both specimen layouts, while the number of cycles at the knee point,

N_k , was found to be higher for the specimens oriented longitudinally to the rolling direction. The difference can be caused by large, in the rolling direction elongated $Al_6(Mn, Fe)$ particles, which cause higher stress concentrations when tested in the TD. Furthermore, the main part of the larger particles has a cuboidal shape, with a larger axis approximately parallel to the rolling direction. Thus, in the RD orientation, the larger axis of particles lay in the direction of the load and in the TD orientation perpendicular to the load. It could be expected that at TD orientation, higher stress concentrations occurred at the particle–matrix interface and that this leads to slightly worse fatigue resistance in the TD direction.

- The micrography of the fractured surfaces of the fatigue specimens has shown that the fracture characteristics are similar for both specimen orientations (longitudinal or transversal). The fracture surface has a typical appearance for the ductile material, characterised by striations during propagation of the fatigue crack and final ductile fracture. The distance between striations increased from the crack beginning (less than 0.5 micrometres) to the crack end (more than 3 micrometres).
- In the proposed research work, we analysed only two specimen orientations: (i) in the rolling direction and (ii) transverse to the rolling direction. The third specimen orientation (45° in regard to the rolling direction) could be investigated in our further research work. Furthermore, further research work should consider the higher number of experiments, especially in the long-life fatigue area (more than 10^7 loading cycles). In this case, a comprehensive statistical evaluation could be performed to obtain more qualitative results regarding the fatigue behaviour of the analysed aluminium alloy.

Author Contributions: Conceptualisation, S.G. and B.N.; methodology, S.G.; validation, S.G.; investigation, B.N., T.V., and F.Z.; writing—original draft preparation, B.N.; writing—review and editing, S.G., F.Z., and T.V.; visualisation, S.G.; supervision, S.G. and F.Z.; project administration, S.G.; All authors have read and agreed to the published version of the manuscript.

Funding: This research was funded by the Slovenian Research Agency (ARRS), Research Core Funding No. P2-0063.

Data Availability Statement: The data presented in this study are available on request from the corresponding author.

Acknowledgments: The authors acknowledge the financial support of the Research Core Funding's (No. P2-0063 and No. P2-0120) from the Slovenian Research Agency. The authors also acknowledge for the use of research equipment "high-frequency pulsator" within the project "Upgrading national research infrastructures—RIUM", which was co-financed by the Republic of Slovenia, the Ministry of Education, Science and Sport and the European Union from the European Regional Development.

Conflicts of Interest: The authors declare no conflict of interest.

References

1. Hirsch, J.; Al-Samman, T. Superior Light Metals by Texture Engineering: Optimised Aluminum and Magnesium Alloys for Automotive Applications. *Acta Mater.* **2013**, *61*, 818–843. [[CrossRef](#)]
2. Liu, Y.; Sun, Y.; Zhang, L.; Zhao, Y.; Wang, J.; Liu, C. Microstructure and Mechanical Properties of Al-5Mg-0.8Mn Alloys with Various Contents of Fe and Si Cast under Near-Rapid Cooling. *Metals* **2017**, *7*, 428. [[CrossRef](#)]
3. Jin, H. Optimization of Aluminum Alloy AA5083 for Superplastic and Quick Plastic Forming. *Metall. Mater. Trans. A* **2019**, *50*, 3868–3890. [[CrossRef](#)]
4. Ilman, M.N.; Triwibowo, N.A.; Wahyudianto, A.; Muslih, M.R. Environmentally Assisted Fatigue Behaviour of Stress Relieved Metal Inert Gas (MIG) AA5083 Welds in 3.5% NaCl Solution. *Int. J. Fatigue* **2017**, *100*, 285–295. [[CrossRef](#)]
5. Billy, R.G.; Müller, D.B. Aluminium Use in Passenger Cars Poses Systemic Challenges for Recycling and GHG Emissions. *Resour. Conserv. Recycl.* **2023**, *190*, 106827. [[CrossRef](#)]
6. Tianyu, Z.; Teng, Z.; Yuting, H.; Xianghong, F.; Yaping, B. Probabilistic Model of the Fatigue Life of Epoxy-Coated Aluminum Alloys Considering Atmospheric Exposure. *Int. J. Fatigue* **2022**, *162*, 106899. [[CrossRef](#)]
7. Raabe, D.; Ponge, D.; Uggowitzer, P.J.; Roscher, M.; Paolantonio, M.; Liu, C.; Antrekowitsch, H.; Kozeschnik, E.; Seidmann, D.; Gault, B.; et al. Making Sustainable Aluminum by Recycling Scrap: The Science of "Dirty" Alloys. *Prog. Mater. Sci.* **2022**, *128*, 100947. [[CrossRef](#)]

8. Hajjioui, E.A.; Bouchaâla, K.; Faqir, M.; Essadiqi, E. A Review of Manufacturing Processes, Mechanical Properties and Precipitations for Aluminum Lithium Alloys Used in Aeronautic Applications. *Heliyon* **2022**, *9*, e12565. [[CrossRef](#)]
9. Manuel, N.; Beltrão, D.; Galvão, I.; Leal, R.M.; Costa, J.D.; Loureiro, A. Influence of Tool Geometry and Process Parameters on Torque, Temperature, and Quality of Friction Stir Welds in Dissimilar Al Alloys. *Materials* **2021**, *14*, 6020. [[CrossRef](#)]
10. Xu, S.; Chen, J.; Shen, W.; Hou, R.; Wu, Y. Fatigue Strength Evaluation of 5059 Aluminum Alloy Welded Joints Considering Welding Deformation and Residual Stress. *Int. J. Fatigue* **2022**, *162*, 106988. [[CrossRef](#)]
11. Bay, R.M.; Shrock, D.J.; Akman, A.M.; Bland, L.G.; Thodla, R.; Lockem, J.S. The effect of sensitization and fatigue loading frequency on corrosion fatigue of AA5083-H131. *Int. J. Fatigue* **2019**, *124*, 1–9. [[CrossRef](#)]
12. Sidhom, N.; Moussa, N.B.; Janeb, S.; Braham, C.; Sidhom, H. Potential Fatigue Strength Improvement of AA 5083-H111 Notched Parts by Wire Brush Hammering: Experimental Analysis and Numerical Simulation. *Mater. Des.* **2014**, *64*, 503–519. [[CrossRef](#)]
13. Liu, Y.; Luo, L.; Han, C.; Ou, L.; Wang, J.; Liu, C. Effect of Fe, Si and Cooling Rate on the Formation of Fe- and Mn-Rich Intermetallics in Al-5Mg-0.8Mn Alloy. *J. Mater. Sci. Technol.* **2016**, *32*, 305–312. [[CrossRef](#)]
14. Ding, S.; Zhang, J.; Khan, S.A.; Yanagimoto, J. Static Recovery of A5083 Aluminum Alloy after a Small Deformation through Various Measuring Approaches. *J. Mater. Sci. Technol.* **2022**, *104*, 202–213. [[CrossRef](#)]
15. Dowling, N.E. *Mechanical Behavior of Materials*; Cambridge University Press: Cambridge, UK, 2000; Volume 15, ISBN 978-0-13-139506-0.
16. Klemenc, J.; Šeruga, D.; Nagode, A.; Nagode, M. Comprehensive Modelling of the Hysteresis Loops and Strain–Energy Density for Low-Cycle Fatigue-Life Predictions of the AZ31 Magnesium Alloy. *Materials* **2019**, *12*, 3692. [[CrossRef](#)] [[PubMed](#)]
17. Tomažinčič, D.; Nečemer, B.; Vesenjāk, M.; Klemenc, J. Low-Cycle Fatigue Life of Thin-Plate Auxetic Cellular Structures Made from Aluminium Alloy 7075-T651. *Fatigue Fract. Eng. Mater. Struct.* **2019**, *42*, 1022–1036. [[CrossRef](#)]
18. Sedighi, M.; Monshi, P.; Joudaki, J. Investigation of Mechanical Properties and Fatigue Life of ECARed AA5083 Aluminium Alloy. *Fatigue Fract. Eng. Mater. Struct.* **2017**, *40*, 412–422. [[CrossRef](#)]
19. Ma, M.; Zhang, J.; Yi, D.; Wang, B. Investigation of High-Cycle Fatigue and Fatigue Crack Propagation Characteristic in 5083-O Aluminum Alloy. *Int. J. Fatigue* **2019**, *126*, 357–368. [[CrossRef](#)]
20. Meng, L.; Goyal, A.; Doquet, V.; Ranc, N.; Couzinié, J.-P. Ultrafine versus Coarse Grained Al 5083 Alloys: From Low-Cycle to Very-High-Cycle Fatigue. *Int. J. Fatigue* **2019**, *121*, 84–97. [[CrossRef](#)]
21. Ben Ali, N.; Estevez, R.; Tanguy, D. Heterogeneity of Grain Boundaries in 5xxx and 7xxx Aluminum Alloys and Its Influence on Intergranular Toughness. *Eng. Fract. Mech.* **2013**, *97*, 1–11. [[CrossRef](#)]
22. Hockauf, K.; Wagner, M.F.-X.; Halle, T.; Niendorf, T.; Hockauf, M.; Lampke, T. Influence of Precipitates on Low-Cycle Fatigue and Crack Growth Behavior in an Ultrafine-Grained Aluminum Alloy. *Acta Mater.* **2014**, *80*, 250–263. [[CrossRef](#)]
23. Wu, Y.; Liao, H.; Tang, Y. Enhanced High-Cycle Fatigue Strength of Al-12Si-4Cu-1.2Mn-T6 Cast Aluminum Alloy at Room Temperature and 350 C. *Mater. Sci. Eng. A* **2021**, *825*, 141917. [[CrossRef](#)]
24. Khisheh, S.; Khalili, K.; Azadi, M.; Hendouabadi, V.Z. Influences of Roughness and Heat Treatment on High-Cycle Bending Fatigue Properties of A380 Aluminum Alloy under Stress-Controlled Cyclic Loading. *Mater. Chem. Phys.* **2021**, *264*, 124475. [[CrossRef](#)]
25. Gao, T.; Sun, Z.; Xue, H.; Retraint, D. Effect of Surface Mechanical Attrition Treatment on High Cycle and Very High Cycle Fatigue of a 7075-T6 Aluminium Alloy. *Int. J. Fatigue* **2020**, *139*, 105798. [[CrossRef](#)]
26. Meng, X.; Leng, X.; Shan, C.; Zhou, L.; Zhou, J.; Huang, S.; Lu, J. Vibration Fatigue Performance Improvement in 2024-T351 Aluminium Alloy by Ultrasonic-Assisted Laser Shock Peening. *Int. J. Fatigue* **2023**, *168*, 107471. [[CrossRef](#)]
27. Xing, S.; Pei, X.; Mei, J.; Dong, P.; Su, S.; Zhen, C. Weld Toe versus Root Fatigue Failure Mode and Governing Parameters: A Study of Aluminium Alloy Load-Carrying Fillet Joints. *Mar. Struct.* **2023**, *88*, 103344. [[CrossRef](#)]
28. Sakin, R. Investigation of Bending Fatigue-Life of Aluminum Sheets Based on Rolling Direction. *Alex. Eng. J.* **2018**, *57*, 35–47. [[CrossRef](#)]
29. Nečemer, B.; Klemenc, J.; Zupanič, F.; Glodež, S. Modelling and Predicting of the LCF-Behaviour of Aluminium Auxetic Structures. *Int. J. Fatigue* **2022**, *156*, 106673. [[CrossRef](#)]
30. Kramberger, J.; Nečemer, B.; Glodež, S. Assessing the Cracking Behavior of Auxetic Cellular Structures by Using Both a Numerical and an Experimental Approach. *Theor. Appl. Fract. Mech.* **2019**, *101*, 17–24. [[CrossRef](#)]
31. Nečemer, B.; Kramberger, J.; Vuherer, T.; Glodež, S. Fatigue Crack Initiation and Propagation in Re-Entrant Auxetic Cellular Structures. *Int. J. Fatigue* **2019**, *126*, 241–247. [[CrossRef](#)]
32. Nečemer, B.; Vuherer, T.; Glodež, S.; Kramberger, J. Fatigue Behaviour of Re-Entrant Auxetic Structures Made of the Aluminium Alloy AA7075-T651. *Thin-Walled Struct.* **2022**, *180*, 109917. [[CrossRef](#)]
33. Nečemer, B.; Zupanič, F.; Gabriel, D.; Tarquino, E.A.; Šraml, M.; Glodež, S. Low Cycle Fatigue Behaviour of Ductile Aluminium Alloys Using the Inelastic Energy Approach. *Mater. Sci. Eng. A* **2021**, *800*, 140385. [[CrossRef](#)]
34. Nečemer, B.; Klemenc, J.; Glodež, S. The Computational LCF-Analyses of Chiral and Re-Entrant Auxetic Structure Using the Direct Cyclic Algorithm. *Mater. Sci. Eng. A* **2020**, *789*, 139618. [[CrossRef](#)]
35. Lehmus, D.; Vesenjāk, M.; de Schampheleire, S.; Fiedler, T. From Stochastic Foam to Designed Structure: Balancing Cost and Performance of Cellular Metals. *Materials* **2017**, *10*, 922. [[CrossRef](#)] [[PubMed](#)]
36. Yen, B.T.; Hodgson, I.C.; Zhou, Y.E.; Crudele, B.B. Bilinear S-N Curves and Equivalent Stress Ranges for Fatigue Life Estimation. *J. Bridg. Eng.* **2013**, *18*, 26–30. [[CrossRef](#)]

37. Tanaka, K.; Akiniwa, Y. A Model for Propagation of Small Fatigue Crack Interacting with Grain Boundary. *J. Soc. Mater. Sci. Jpn.* **1985**, *34*, 1301–1307. [[CrossRef](#)]
38. Tanaka, K. Fatigue Crack Propagation. In *Comprehensive Structural Integrity*; Milne, I., Ritchie, R.O., Karihaloo, B., Eds.; Pergamon: Oxford, UK, 2003.
39. Pineau, A.; McDowell, D.L.; Busso, E.P.; Antolovich, S.D. Failure of Metals II: Fatigue. *Acta Mater.* **2016**, *107*, 484–507. [[CrossRef](#)]

Disclaimer/Publisher's Note: The statements, opinions and data contained in all publications are solely those of the individual author(s) and contributor(s) and not of MDPI and/or the editor(s). MDPI and/or the editor(s) disclaim responsibility for any injury to people or property resulting from any ideas, methods, instructions or products referred to in the content.